Evidencing non-Bloch dynamics in temporal topolectrical circuits

Maopeng Wu,[1] Qian Zhao,[1,*] Lei Kang,[2] Mingze Weng,[1] Zhonghai Chi,[1] Ruiguang Peng,[1] Jingquan Liu,[3] Douglas H. Werner,[2] Yonggang Meng,[1] and Ji Zhou[4]

[1]*State Key Laboratory of Tribology, Department of Mechanical Engineering, Tsinghua University, Beijing 100084, China*
[2]*Department of Electrical Engineering, The Pennsylvania State University, University Park, Pennsylvania 16802, USA*
[3]*Department of Engineering Physics, Tsinghua University, Beijing 100084, China*
[4]*State Key Laboratory of New Ceramics and Fine Processing, School of Materials Science and Engineering, Tsinghua University, Beijing 100084, China*

(Received 17 December 2021; revised 27 December 2022; accepted 2 February 2023; published 21 February 2023)

One of the core concepts from the non-Hermitian skin effect is the extended complex wave vectors (CW) in the generalized Brillouin zone (GBZ), while the origin of CW remains elusive, and further experimental demonstration of GBZ is still lacking. We show that the bulk states of an open system dynamically governed by the Lindblad master equation exhibit non-Bloch evolution which results in CW. Experimentally, we present temporal topolectrical circuits to serve as simulators for the dynamics of an open system. By reconstructing the correspondence between the bulk states of an open system and circuit voltage modes through gauge scale potentials in the circuit, the non-Bloch evolution is demonstrated. Facilitated by the simulators and proper approach to characterize the non-Bloch band proposed here, the GBZ is confirmed. Our work may advance the investigation of the dissipative topological modes and provide a versatile platform for exploring the unique evolution and topology for both closed and open systems.

DOI: 10.1103/PhysRevB.107.064307

I. INTRODUCTION

In topological matter [1–4], the number of topological surface states is usually related to the topological structure of bulk states (or topological invariances), which is summarized as the bulk-boundary correspondences (BBCs). Recently, those topological phase studies have been generalized to the systems with non-Hermitian (NH) Hamiltonians [5–7], which usually root in the intrinsic dissipative property (e.g., inelastic-scattering-induced finite quasiparticle lifetime [8–10], material gain/loss [11,12], resonator Q factor [13,14], asymmetric hopping amplitudes [15–17], and complex coupling [18]) or interaction with the surrounding environments (e.g., Liouvillian dissipators [19,20]). The interplay between non-Hermiticity and topological boundaries has attracted intense interest, not only because of the exotic phenomena, such as the delocalizing topological modes [21–23], but also because of the potential for exciting applications, such as the NH laser [24,25], the light steering device [26].

Nevertheless, recent studies show that reported BBC theories for Hermitian systems are not well defined in NH systems. Subsequent investigations revealed that a broad range of NH models inherently exhibit the non-Hermitian skin effect (NHSE) [23,27–37], which can be captured mathematically by complex wave vectors (CW). Namely, the bulk eigenstates of the NH Hamiltonian do not extend over the systems but prefer exponentially localizing (or piling up) at its boundaries. Accordingly, the Bloch theorem is generalized to $\psi_{\tilde{\mathbf{k}}}(\mathbf{r}) = e^{i\tilde{\mathbf{k}}\cdot\mathbf{r}} u_{\tilde{\mathbf{k}}}(\mathbf{r})$, where $\tilde{\mathbf{k}}$ belongs to the generalized Brillouin zone (GBZ) [28,34,38–42]. The GBZ provides an amendment that deals with anomalous BBC by replacing $e^{i\mathbf{k}}$ with $e^{i\tilde{\mathbf{k}}}$ in calculating the topological invariants, e.g., the paradigmatic one-dimensional NH SSH model [28,43] as experimentally demonstrated in [44], NH Chern insulators [45], NH second-order topological insulators [46], and so on. However, the underlying physical mechanism of this phenomenon-driven development of CW remains elusive. Furthermore, owing to the lack of an appropriate approach to characterize the non-Bloch band, the GBZ has not been experimentally demonstrated.

In this work we investigate a second-order topological insulator that interacts with the environment, and thereby its time evolution follows the Lindblad master equation. We show the time evolution of the bulk field experiences an additional space-related negative damping term beyond Bloch theorem (dubbed the non-Bloch evolution), which leads to CW. Also, the concept of topolectrical circuits is adapted to emulate the non-Bloch evolution. By contrast, the gauge scale potentials in the proposed circuits bridge the bulk field and the voltage modes, which lay the necessary basis for emulating. Moreover, we reveal that Laplace transform rather than Fourier transform connects the reciprocal space and the real lattice space for non-Bloch problems, indicating an unexplored avenue to characterize the non-Bloch band. The above revelation, together with the proposed circuits, finally allows us to verify the existence of the GBZ experimentally. Importantly, the measurement of the circuit impedance response allows us to experimentally verify that the second-order topological invariance derived from the non-Bloch band.

In a separate work [47], we apply temporal topolectrical circuits to directly observe the nodal-line conversion

*zhaoqian@tsinghua.edu.cn

(including node-line [48] conversion and non-Abelian line-line conversion [49]) determined by the relative homotopy, which cannot be reached by other platforms.

II. NON-BLOCH EVOLUTION IN OPEN SYSTEMS

Following the Lindblad master equation [50], the time evolution of a reduced density matrix ρ of an open system is governed by

$$\frac{d\rho}{dt} = -i[H_0, \rho] + \sum_u (2L_u\rho L_u^\dagger - \{L_u^\dagger L_u, \rho\}), \tag{1}$$

where H_0 is the Hermitian Hamiltonian of the original system. L_u is the set of dissipators due to environment and with the translational symmetry L_u can be simplified as $L_u = \{L_{\mathbf{k}}^g, L_{\mathbf{k}}^l\}$ in the Brillouin zone (BZ), which includes the particle gain $L_{\mathbf{k}}^g = \psi_{\mathbf{k}}^\dagger D_{\mathbf{k}}^g$ and the loss $L_{\mathbf{k}}^l = D_{\mathbf{k}}^l \psi_{\mathbf{k}}$, $\psi_{\mathbf{k}} = (a_{\mathbf{k},1}, a_{\mathbf{k},2}, ..., a_{\mathbf{k},n})^T$, $a_{\mathbf{k},i}$ is the annihilation operator, and n represents the degrees of freedom per unit cell (a concrete model, see Appendix A). We further assume the element constitutions are bosons which are distinct from the fermions in the commutation relation [51]. The field coherences $\phi_{\mathbf{k},i}(t) = \langle a_{\mathbf{k},i}(t)\rangle = \mathrm{Tr}[a_{\mathbf{k},i}\rho(t)]$ are employed to monitor the time evolution of ρ because of its accessibility. Equation (1) implies that $\phi_{\mathbf{k},i}(t)$ evolves under an effective NH Hamiltonian H:

$$\frac{d\phi_{\mathbf{k},i}}{dt} = -i\sum_m H_{m,n}\phi_{\mathbf{k},j}$$

$$H = H_0 + \frac{i}{2}\left(\left(D_{\mathbf{k}}^{g\dagger} D_{\mathbf{k}}^g\right)^T - D_{\mathbf{k}}^{l\dagger} D_{\mathbf{k}}^l\right). \tag{2}$$

For more details see the Supplemental Material (SM) [52]. Above all, we have the eigenmodes of the field coherences $\phi_{\mathbf{k},n}(t)$:

$$\phi_{\mathbf{k},n}(t) = \Phi_{\mathbf{k},n} e^{iE_n(\mathbf{k})t - i\mathbf{k}\cdot\mathbf{r}}, \tag{3}$$

where $\Phi_{\mathbf{k},n}$ and $E_n(\mathbf{k})$ are the eigenvectors and eigenvalues of H, respectively. Notably, H reduces to H_0 in the absence of the coupling.

Without loss of generality, we consider a two-dimensional (2D) system consisting of four orbitals arranged on a square lattice [Fig. 1(b)]. This nondissipating model has been used to study the higher-order topological corner states [53–55]. Heuristically, we note that, to construct an intriguing model that exhibits the non-Bloch evolution and hosts the topological corner states, the dissipators should have the following properties: (i) ensure H is NH, $H \neq H^\dagger$, (ii) introduce certain (i.e., asymmetric) hopping between the orbitals to enable non-Bloch behavior; and (iii) ensure H respects certain symmetry to allow the topological phase. Regarding those properties, the dissipators considered here are

$$D_{\mathbf{k}}^g = 2\sqrt{\gamma}\begin{pmatrix} 1 & & & \\ & 1 & & \\ & & 1 & \\ & & & 1 \end{pmatrix},$$

$$D_{\mathbf{k}}^l = \sqrt{2\gamma}\begin{pmatrix} 1 & & -i & \\ & 1 & & i \\ & -i & 1 & \\ -i & & & 1 \end{pmatrix}, \tag{4}$$

and therefore

$$H = [t + \lambda\cos(k_x)]\tau_x\sigma_0 - [\lambda\sin(k_x) + i\gamma]\tau_y\sigma_z + [t + \lambda\cos(k_y)]\tau_y\sigma_y + [\lambda\sin(k_y) + i\gamma]\tau_y\sigma_x, \tag{5}$$

where $(t, -t)$ and $(\lambda, -\lambda)$ are the intracell and intercell hopping, respectively, and τ_i and σ_i $(i = x, y, z)$ are Pauli matrices. To present a physical picture of the effective NH Hamiltonian H, we transform it back into real space shown in Fig. 1(b). The interactions L_u between the original system and the environment can be interpreted as asymmetric intracell hopping, which accounts for a complex flux threading the unit cell.

Our calculation shows that *bulk* field coherences of an excitation (like a photon) centered at the lattice prefer to evolve toward the specific direction, while evolution along the opposite direction is suppressed. In other words, field coherences experience a negative space-related damping term during the evolution, which behaves as the increasing number of excitation along the direction it prefers. In an electromagnetic system, media such as band-gap materials can block some specific modes, resulting in a spatial concentration of those modes around the medium's surface (i.e., the electromagnetic skin effect). In stark contrast, in the proposed NH systems, the eigenmodes of the bulk field coherences can propagate but still exhibit the skin effect. Therefore in the dynamics of $\phi_{\mathbf{k},n}$, we focus on the bulk eigenmodes. The damping term is independent of boundary condition, quite different from the eigenvalue spectrum that shows great sensitivity to the boundaries. Even so, the system with periodic boundary conditions never reaches a steady state, as the field coherences will exponentially and constantly accumulate along the periodic direction. We remark that the CW caused by non-Bloch evolution is independent of quantum coherence, which gives rise to a possibility of emulating the evolution with classical circuits. In fact, the NHSE (described by CW) may dramatically shape the long-time Lindblad dynamics after the jump [51].

III. EMULATING NON-BLOCH DYNAMICS WITH TEMPORAL TOPOLECTRICAL CIRCUITS

For the circuit in a lattice structure [56], its admittance matrix in the BZ can be described as $J(w, \mathbf{k}) = YI + J_0(w, \mathbf{k})$, where the diagonal elements YI (so-called self-admittances) are preset to be identical. The node voltages $V_{\mathbf{k},0}(t)$ that change over time are (see SM [52])

$$V_{\mathbf{k}}(t) = \mathbf{V}_{\mathbf{k},0}\, e^{i\omega(\mathbf{k})t - i\mathbf{k}\cdot\mathbf{r}}, \tag{6}$$

where $\mathbf{V}_{\mathbf{k},0}$ are the eigenvectors of $J(w, \mathbf{k})$ with respect to the *zero-value eigenvalues*, and w is the resonant frequency of the circuit. The above equation reminds us of Eq. (3) and indicates that the response of the node voltage can potentially emulate the evolution of the field coherences, as long as $J(w, \mathbf{k})$ is appropriately configured to be of the same form as that of H [a little different from Eq. (3), and we will solve this with gauge scale potentials].

The unit cell of the circuit designed to emulate $\phi_{\mathbf{k},i}(t)$ is specified in Fig. 1(c). Capacitor-inductor pairs (C_t, L_t) and (C_λ, L_λ) are used to emulate the intracell and intercell hopping of H. $C_\lambda = \lambda C_t$ and $L_\lambda = L_t/\lambda$ so that the pairs have the same LC resonant frequency w_0. Furthermore, we

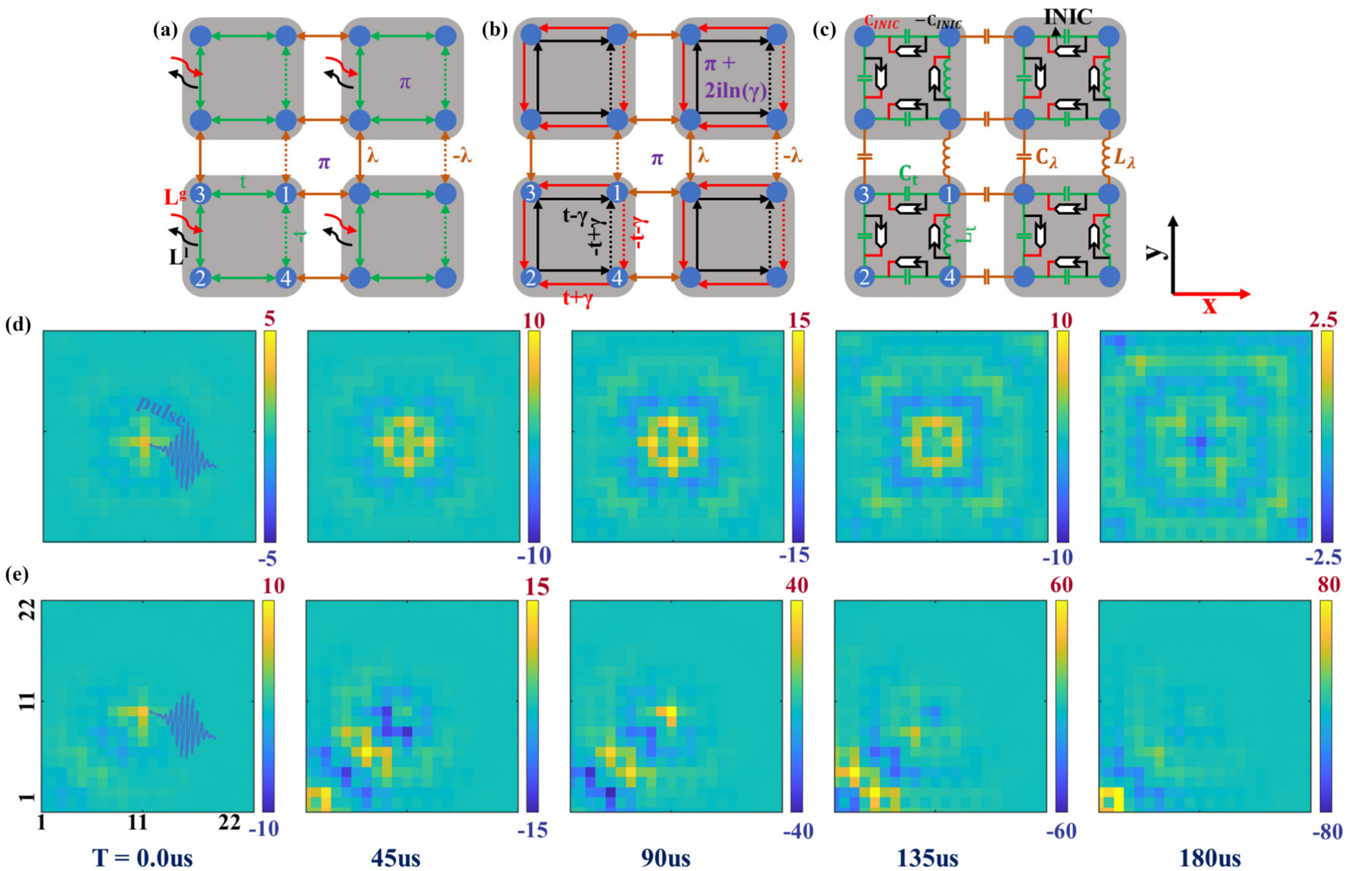

FIG. 1. Non-Bloch evolution and its demonstration using a temporal topolectrical circuit. (a) Tight-binding representation of the model. Each unit cell contains four orbitals (solid blue circles). The green and brown arrows denote the intercell and intracell hopping, respectively. The dashed arrows have a relative negative sign to account for a flux of π threading each plaquette. The dissipators L^l and L^g describe the boson loss and gain in a unit cell. (b) The effective Hamiltonian H for $\phi_{\mathbf{k},i}(t)$ in real space. The red and black arrows represent the asymmetric intracell hopping, accounting for an imaginary flux $2iln(\gamma)$. (b) Temporal topolectrical circuit realization of the non-Bloch evolution. $(C_t, L_t) = (10\text{ nF}, 30\ \mu\text{H})$, $\lambda = 2$, $\gamma = 0.5$. The configuration of $Y_0 = iw_0C_0$, $C_0 = 33$ nF is not plotted for clarity. (c) Measured time-resolved voltage signal of the Hermitian topolectrical circuit (11×11 units) after the pulse. The node voltage of the bulk modes propagates in all directions and behaves as a Bloch wave with forming a quasicylindrical wave front. (d) Time-resolved voltage signal of the NH circuit after pulse. In contrast, the node voltage propagates chirally toward the corner with the increasing amplitude, confirming the non-Bloch dynamics. Note that the chirality of the non-Bloch wave is controlled by the dissipators.

implement the negative impedance converters with current inversion (INIC), which served as an indictor of the coupling between the system and the environment (see SM [52]). Each node is grounded via passive elements to guarantee the self-admittance $Y = Y_0\tau_0\sigma_0$. The admittance matrix $J(w_0, \mathbf{k})$ of the resulting circuit reads

$$(iw_0C_t)^{-1}J(w_0, \mathbf{k}) = Y_0\tau_0\sigma_0 + H. \tag{7}$$

Neglecting the constant prefactor, H and $J(w_0, \mathbf{k})$ take the same form when $Y_0\tau_0\sigma_0 = 0$; nevertheless, as we will see, $Y_0\tau_0\sigma_0 \neq 0$ is essential in our temporal circuit.

The existing topolectrical circuit [57–66] has severe limitations preventing us from exploring non-Bloch evolution and further GBZ. For normal metamaterials or photonic crystals [3,4,67,68], the frequency dimension plays a similar role as the eigenenergy of a solid. However, to keep $J(w_0, \mathbf{k})$ the same form as H, the circuit has to operate at w_0. Besides, the voltage response $V_\mathbf{k}(t)$ [emulating $\phi_{\mathbf{k},n}(t)$] is modeled by $\mathbf{V}_{\mathbf{k},0}$ with vanishing eigenvalue [Eq. (6)], while in most cases, the eigenvalue of $\phi_{\mathbf{k},n}(t)$ usually is not zero. Here, we find Y_0 functions as the gauge scalar potentials (see SM [52]). So one can tune the eigenvalue spectrum with the Y_0 [Fig. 2(a)], just like tuning Fermi energy with chemical potentials. Note that each node of the circuit has a different grounded configuration such that the self-admittances Y_0 (diagonal terms of the admittance matrix) are identical. In other words, one can select the evolution of the bulk field coherences $\phi_{\mathbf{k},n}(t)$ with tuning Y_0. As we will see, Y_0 does more than selecting modes, and it also plays an essential role in GBZ demonstration.

Experimentally, to excite a *bulk* excitation, a current pulse signal with Gaussian form is injected into the center of the circuit (Fig. 3). For direct comparison, the same experiment was also carried out in a Hermitian circuit. Clearly, in the NH system [Fig. 1(e)] the field coherences represented by the voltage response propagate toward the bottom-left corner of the lattice with a negative damping factor (the amplitude increases as a function of the distance). This is in sharp contrast to the symmetric propagation phenomenon (referred as Bloch evolution) observed in a normal Hermitian system [Fig. 1(d)].

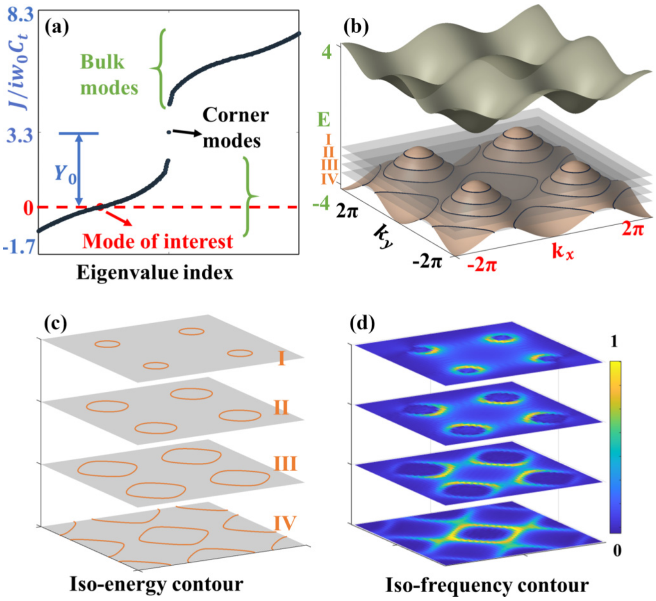

FIG. 2. Selecting the time evolution pattern by adjusting the gauge scalar potentials Y_0 and $\boldsymbol{Y_O}$-enabled FTFS for Bloch band. (a) Eigenvalue spectrum of the circuit admittance matrix $J(w, \mathbf{k})$. The red dot denotes the bulk modes whose eigenvalues are zero. The spectrum is gauge invariant against the diagonal term $Y_0\tau_0\sigma_0$ of $J(w, \mathbf{k})$, and hence it shifts the spectrum upwards by $Y_0 = iw_0C_0$, $C_0 = 33\,\text{nF}$. (b)–(d) Characterizing circuit band by tuning Y_0. (b) Band structure of H with $\gamma = 0$ (Hermitian case), which corresponds to $J(w, \mathbf{k})$. I–IV denote the cut plane with $E = 1.8$, 2.3, 2.8, and 3.3, respectively. Their intersections with the band are the isoenergy contours, which are individually shown in (c). (d) Voltage distribution of the Hermitian circuit (21 by 21 units) in BZ after the Fourier transform with $C_0 = 18\,\text{nF}$, 23 nF, 28 nF, and 33 nF, respectively (for more details see SM [52]).

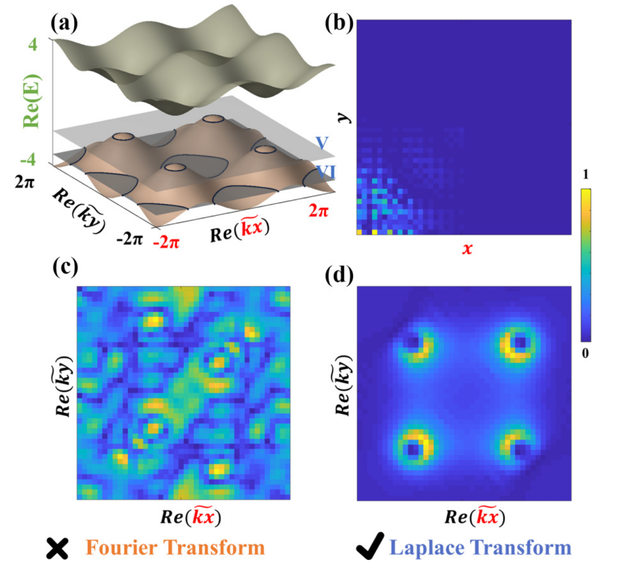

FIG. 4. Failure of the FTFS for a non-Bloch band and characterizing the non-Bloch band with Laplace transform. (a) Non-Bloch band of H with $\gamma = 0.5$. V and VI denote the cut plane with $E = 1.8$ and 3.3, respectively. (b) Calculated voltage response due to a centered point source (not shown) in real space ($C_0 = 18\,\text{nF}$). (c) Corresponding voltage distribution in BZ after the Fourier transform. Clearly, a Fourier transform cannot be used to characterize the non-Bloch band. (d) Corresponding voltage distribution in GBZ after the Laplace transform. The distribution is in great accord with the isocontour [V in (a)]. As for VI, see Fig. 5(d).

IV. GBZ DEMONSTRATION

The Gauge scalar potentials Y_0 also enable an alternating approach to character the circuit band, opening up possibilities for the demonstration of GBZ. In traditional circuits, the circuit bands are obtained through the (or block) diagonalization of the measured impedance matrix. The diagonalization approach has tremendous convenience in studying the sensitivity of the spectrums [59,63], but it fails in demonstrating GBZ as GBZ is a prerequisite in the diagonalization process. The desired approach is the Fourier-transformed field scan (FTFS) if the field distribution (e.g., field coherences) is accessible. FTFS is widely used in artificial crystals and metamaterials, such as [69–71]. As mentioned above, the bulk field distribution is accessible and can be selected at will by adjusting Y_0, thus enabling FTFS to character the *Bloch* circuit band [Figs. 2(b)–2(d)].

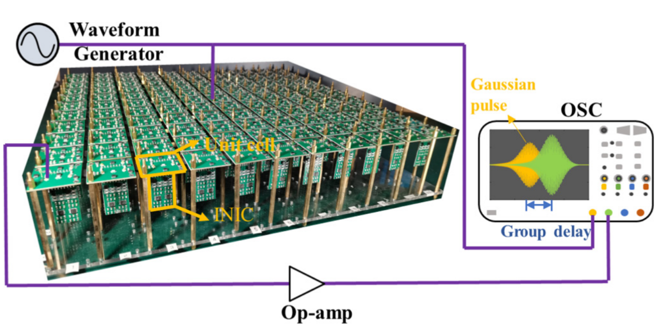

FIG. 3. Schematic of the measurement setup with a photo of the fabricated circuit. Orange rectangles denote a single cell module emulating the original Hermitian system and an INIC module dominating the coupling between the systems and the environment, respectively. Each module is assembled by pin header connectors. Note that the modular design strategy dramatically facilitates circuit debugging and calibration. The oscilloscope (OSC) records the node voltage variation over time.

FTFS is not applicable for the *non-Bloch* band. Without NHSE, FTFS allows one to retrieve the band structure by applying the Fourier transform to the measured spatial field patterns [see Figs. 2(b)–2(d), and to avoid NHSE we take $\gamma = 0$]. Because the degeneracy modes with identical eigenenergy are simultaneously excited, the obtained distribution in momentum space is the iso-energy contour of the band. However, Fourier transforms of the non-Bloch wave are divergent when FTFS is applied [Fig. 4(c)]. This divergence arises from the limitation of the Dirichlet conditions [72]. Therefore FTFS is still far from demonstrating GBZ (also see Appendix B).

For non-Bloch problems, we find that the Laplace transform rather than Fourier transform can map eigenvectors in real space to that in GBZ [Fig. 4(d)]. In order to make a convergent transformation, an exponential decay (or growth) factor is usually introduced to the integral kennel, leading to the $e^{i\tilde{\mathbf{k}}\cdot\mathbf{r}} \rightarrow e^{\mathbf{s}\cdot\mathbf{r}}$, $\mathbf{s} \subset \mathbb{C}$. This is well known as the bilateral

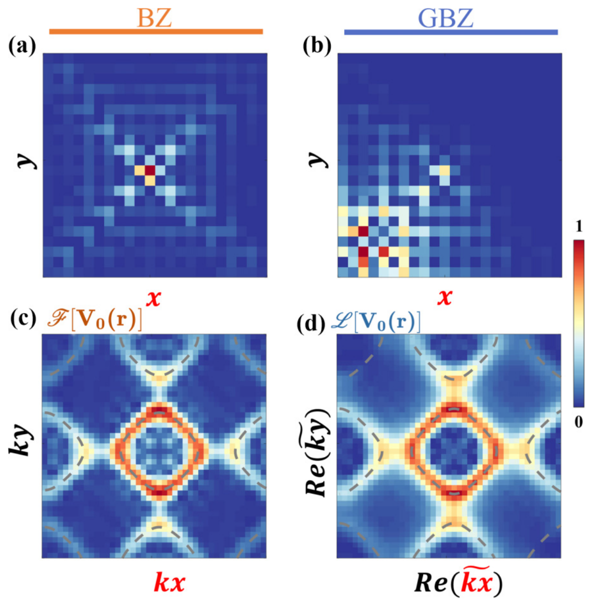

FIG. 5. Experimental demonstration of GBZ. (a), (c) Measured voltage distribution (due to a centered point source) of the Hermitian system in real space and its isofrequency contour after Fourier transform. (b), (d) Measured voltage distribution of the NH system in real space and its isofrequency contour after the Laplace transform. The voltage distribution in (d) is localized at the corner as a result of the NHSE. Gray dash lines indicate the calculated contour. For more numerical data see Appendix B.

Laplace transformation (more details see Appendix B). In our generalized theory, we interpret the complex argument $\mathbf{s}$ is as CW, then accordingly, the Laplace transformation decomposes the wave function $\psi_n(\mathbf{r})$ in real space into that in GBZ:

$$\psi_n'(\tilde{\mathbf{k}}) = \mathscr{L}[\psi_n(\mathbf{r})] = \int_{\mathbf{r}} \psi_n e^{i\tilde{\mathbf{k}}\cdot\mathbf{r}} d\mathbf{r}. \tag{8}$$

Figures 5(b) and 5(d) present the measured voltage distribution and the voltage profile after the Laplace transformation, which is in great agreement with the theoretical analysis (for more data about GBZ demonstration, see the SM [52]). As a control for GBZ, we also measure the voltage field distribution of the Hermitian systems ($\gamma = 0$) and transform it into momentum space using the Fourier transform [Figs. 5(a) and 5(c)]. Clearly, GBZ is experimentally demonstrated. Here, the $H(\tilde{\mathbf{k}})$ in GBZ is assumed in the calculation of the non-Bloch band shown in Fig. 4(a), and the non-Bloch band is obtained by analytic continuation [73]: $H(\mathbf{k}) \to H(\tilde{\mathbf{k}})$, $\tilde{\mathbf{k}} \in$ GBZ. This assumption is based on real space and guarantees the energy levels are continuous for a large open lattice [38].

V. EXPERIMENTALLY DEMONSTRATING TOPOLOGY REDEFINED IN GBZ

As stated above, we revealed how the NHSE and the GBZ arise due to non-Bloch dynamics. In this section we demonstrate that the GBZ leads to the generalized topological invariance of the NH Hamiltonian in complex momentum space. As an insight into the generalized topology, we calculate second-order topology diagrams for our model associated with the Bloch band [Fig. 6(a)] according to [53] and the non-Bloch band [Fig. 6(b)] according to [46]. As shown in Fig. 6, the Bloch and the non-Bloch topological phase diagrams of the second order are significantly different. In particular, the non-Bloch diagram predicts the topologically trivial phase when $(\gamma, \lambda) = (0.6, 0.6)$, while the Bloch one exhibits a topological phase under the same conditions.

With the appropriate configuration, the impedance resonance of the topolectrical circuit consistently indicates the presence of corner states, which allows us to identify the correct phase diagram experimentally. On the one hand, the impedance response Z_{a0} at node a against the ground can be acquired mathematically by inverse as shown in Eq. (6) (see SM [52]):

$$Z_{a0}(w) = J_{a0}(w)^{-1} = \sum_n \frac{\psi_{n,a}\phi^*_{n,a}}{j_n}, \tag{9}$$

where $\psi_{n,a}$ and $\phi_{n,a}$ are the nth right and left eigenvectors of $J_{a0}(w)$, which obey the biorthogonal normalization condition $\langle \phi_{n,a}|\psi_{m,a}\rangle = \delta_{nm}$. The impedance Z_{a0} becomes infinite if there exists a finite density of nonvanishing eigenmodes with $j_n = 0$. In practical systems, owing to parasitic resistances, such divergences (infinite Z_{a0}) appear as impedance resonances rather than infinity. On the other hand, the eigenvalues of topological corner states, which are located at the band gap, are always pinned at zero if the onsite potential on each site vanishes, which is predetermined by the chiral symmetry of the Hamiltonian. Therefore the impedance peak around the corner at the resonant frequency is a definite and reliable indicator of the presence of corner states. We remark that this one-to-one correspondence follows the exiting topolectrical circuits [59,63], but the special time domain property of our circuits, which is crucial for evidencing the non-Bloch evolution and GBZ demonstration, cannot be found there. Figure 6(c) plots a comparison between the measured results and the simulations from LTSPICE. A strong impedance resonance peak is identified when $(\gamma, \lambda) = (0.6, 0.6)$, revealing not only the breakdown of the conventional BBC, but also that the non-Bloch topological invariance can precisely predict the corner modes.

VI. CONCLUSION

Non-Hermitian systems promise a pathway to expand the parameter space (such as complex wave vectors) into the complex realm. Here we show that the non-Bloch evolution of the open systems can result in complex wave vectors and experimentally demonstrate the GBZ, which accommodates the complex wave vectors. The temporal topolectrical circuit developed in our work provides a simple-to-realize platform to study the dynamics and topology of open quantum systems (and of course closed systems, such as [47]). Our works could advance the application of topological systems, such as topological lasers whose topological lasing modes extend over the bulk or directional amplification with excellent isolation.

Note added. We recently became aware of works which study the hybrid higher-order [74], interaction-induced [75] skin effect, and second-order skin effects identified by machine learning [76].

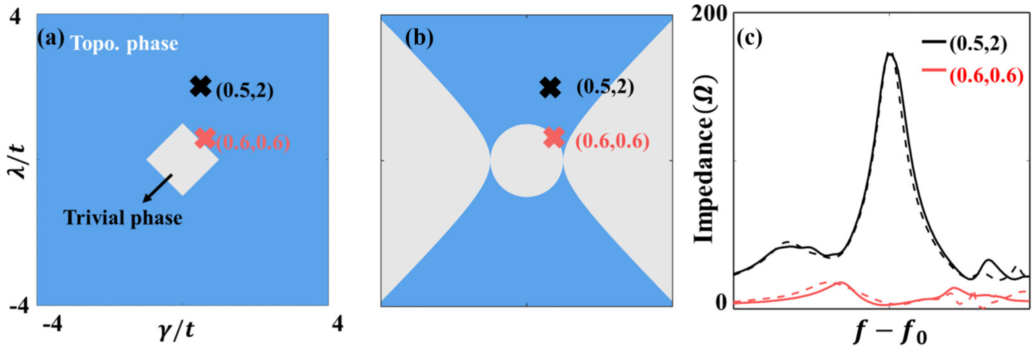

FIG. 6. Experimental demonstration of BBC breakdown and the redefined topology. (a) Bloch second-order topological phase diagram without considering the NH corner effect. (b) Non-Bloch second-order topological phase diagram defined over a closed manifold in complex momentum space. The gray region represents the topologically trivial phase, while the blue region represents the second-order topological phase that hosts corner states. As for $(\gamma, \lambda) = (0.5, 2)$, both diagrams predict the topological phase, while they contradict each other for $(\gamma, \lambda) = (0.6, 0.6)$. (c) Frequency scan of the impedance against ground at the bottom-left corner of the lattice. Solid lines denote the measurement, and dash lines denote the results from LTSPICE simulation. The results indicate that the phase is topological for $(\gamma, \lambda) = (0.5, 2)$ and trivial for $(\gamma, \lambda) = (0.6, 0.6)$, suggesting the second-order non-Bloch topology. The self-admittance $Y_0\tau_0\sigma_0$ is set to be zero such that the admittance matrix $J(w, \mathbf{k})$ respects chiral symmetry. For more data, see Appendix D

ACKNOWLEDGMENTS

The authors thank Zhong Wang, Zhesen Yang, Ce Shang, Fuli Zhang, Yuancheng Fan, Nianhai Shen, and Peng Zhang for useful discussions and suggestions. Funding: This work is supported by the National Natural Science Foundation of China (Grants No. 52273296 and No. 51872154), the Beijing Municipal Science & Technology Commission, and the Administrative Commission of Zhongguancun Science Park No. Z221100006722016.

APPENDIX A: CONCRETE MODELS

Here we give a concrete and intuitive model of ultracold atoms described by Eq. (1) to show the correspondence between the cold atom model and circuits. This is not the central work of our paper and is largely based on Refs. [15,46,53,77,78].

The key idea is introducing effect hopping (including Hermitian and non-Hermitian hopping) between two isolated atoms (or atom clusters) by an auxiliary state [Fig. 7(a)]. To illustrate that consider two isolated states $|\omega\rangle$, and each state couples to a third auxiliary state $|\Delta\rangle$ with amplitudes Ω and $\Omega e^{i\theta}$, respectively. The resulting Hamiltonian reads

$$H = \begin{pmatrix} \omega & 0 & \Omega \\ 0 & \omega & ke^{i\theta} \\ \Omega & e^{-i\theta} & \Delta \end{pmatrix}, \tag{A1}$$

where we set $\Delta = \Omega^2/\omega - \omega$ for the sake of simplicity. Assuming $\omega \ll \Omega$, we find two interesting eigenmodes of H: $(e^{i\theta}, 1, -2\omega/\Omega \approx 0)^{\mathrm{T}}$ and $(1, -e^{-i\theta}, 0)^{\mathrm{T}}$ corresponding to eigenvalue $-w$ and w, respectively. If we neglect the auxiliary states, those eigenmodes are effectively described by

$$H_{\text{eff}} = \begin{pmatrix} 0 & \omega e^{i\theta} \\ \omega e^{-i\theta} & 0 \end{pmatrix}. \tag{A2}$$

Thus an effect Hermitian hopping $\omega e^{i\theta}$ with an Aharonov-Bohm phase between two states is realized.

Note that we can realize a non-Hermitian effect hopping (e.g., asymmetric hopping) if $|\Delta\rangle$ has a finite lifetime. Considering the dissipation of the auxiliary state, the Lindblad master equation of the system shown in Fig. 7(a) reads

$$\frac{d\rho}{dt} = -i[H, \rho] + \alpha(2a_3\rho a_3^\dagger - \{a_3^\dagger a_3, \rho\}), \tag{A3}$$

where a_3 is the annihilation operator in the auxiliary, and α is the decay rate. If we ignore the fast decay mode in the auxiliary, at mean-field level the dynamics is governed by the effect of the non-Hermitian Hamiltonian

$$H_{\text{eff}} = H - i\gamma L^\dagger L, \tag{A4}$$

$$L = a_1 + ia_2, \tag{A5}$$

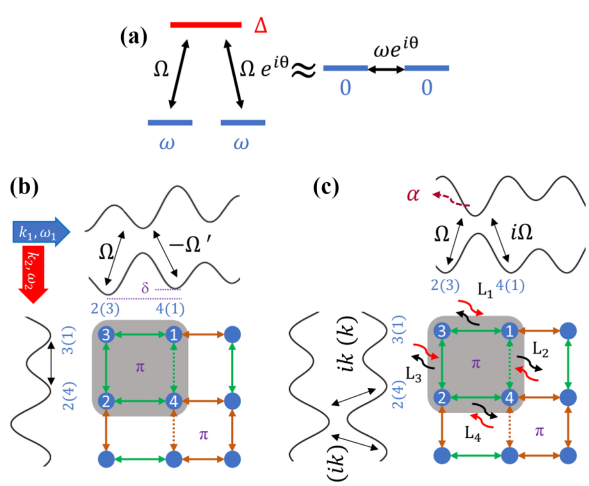

FIG. 7. Model of cold atoms. (a) Induced effect hopping with Aharonov-Bohm phase between two isolated states $|\omega\rangle$. (b) Hermitian limit H_0. A pair of running waves $(\mathbf{k}_i, \omega_i)$ $(i = 1, 2)$ is injected to restore the tunneling. (c) Dissipators L_u. The applied running waves are not shown for simplicity.

where $\gamma = \Omega^2/2\alpha$. The Hamiltonian $H_{\rm eff}$ has asymmetric hopping terms that break Hermiticity.

Hermitian limit H_0 with $\gamma = 0$. Figure 7(b) shows the optical lattice created by three mutually orthogonal standing waves. A magnetic field gradient along x generates a uniform energy offset δ between neighboring sites such that tunneling is forbidden. The effect of tunneling is restored by a pair of running waves $(\mathbf{k}_i, \omega_i)$ $(i = 1, 2)$. The local optical potential created by the waves is proportional to

$$\cos^2\left(\frac{\mathbf{k_1}-\mathbf{k_2}}{2}\cdot\mathbf{r}+\frac{\omega_1-\omega_2}{2}t\right). \tag{A6}$$

The time-dependent term of the potential gives the coupling Ω (Ω') between states and the auxiliary state due to Rabi oscillation, while the rest spatial term leads to the spatially dependent coupling phases (e.g., $e^{i\pi}$). Here we use two LC pairs (C_t, L_t) and (C_λ, L_λ) to realize such lattices.

Dissipators L_u. A similar setup can apply to construct dissipators, and the difference from above is that we assume the auxiliary states dissipate at a rate of α [Fig. 7(c)]. If we ignore the fast decay modes in the auxiliary, we can obtain the master equation of Eq. (1), where

$$\begin{aligned} L_1 &= \sqrt{2\gamma}(a_3 + ia_1), L_2 = \sqrt{2\gamma}(a_1 + ia_4), \\ L_3 &= \sqrt{2\gamma}(a_2 + ia_3), L_4 = \sqrt{2\gamma}(a_2 + ia_4), \end{aligned} \tag{A7}$$

where $\gamma = \Omega^2/(2\alpha)$ and $D^l_{\mathbf{k}} = \sum_{i=1}^4 L_i^\dagger L_i$. In the main article, we also consider a uniform pump $D^g_{\mathbf{k}}$ to cancel for the background loss induced by the L_i $(i = 1, ..., 4)$. We use INIC to emulate the dissipators.

APPENDIX B: REVIEW OF LAPLACE TRANSFORM

For the sake of simplicity, we only consider one-dimensional systems. The integral transform can be easily generalized to high dimensions by replacing $kx \to \mathbf{k}\cdot\mathbf{r}$.

Fourier transform. The Fourier transform of $f(x)$ is defined by

$$\mathscr{F}[f(x)] = \frac{1}{\sqrt{2\pi}}\int_{-\infty}^{\infty} e^{-ikx} f(x)dx. \tag{B1}$$

$\mathscr{F}[f(x)]$ exits if $f(x)$ satisfies Dirichlet's conditions:

(1) $f(x)$ has only a finite number of finite discontinuities and has no infinite discontinuities;

(2) $f(x)$ has only a finite number of maxima and minima;

(3) $f(x)$ is absolutely integrable: $\int_{-\infty}^{\infty}|f(x)|dx < \infty$.

The Fourier transform $\mathscr{F}[\psi_{\tilde{k}}(r)]$ for the states $\psi_{\tilde{k}}(r)$ with complex wave numbers $\tilde{k}$ does not exist, as the states are not absolutely integrable [also see Fig. 4(c)].

Laplace transform. Based on the Fourier transform, the bilateral Laplace transform is defined as

$$\mathscr{L}[f(x)] = \int_{-\infty}^{\infty} s^{-sx} f(x)dx, \tag{B2}$$

where s is the transform variable which is a complex number. The definition differs slightly from the unilateral Fourier transform, whose integral interval is $[0, \infty)$. This difference comes from the fact that in engineering and other sciences one can always set $f(x) = 0$ in $(-\infty, 0]$, but for the skin effect problem, $f(x) \neq 0$ in $(-\infty, 0]$. Besides the Dirichlet's conditions, the existence of the Laplace transform requires $f(x)$ to be of exponential order a: $|f(x)| \leqslant \xi e^{ax}$, if there exists a positive constant ξ.

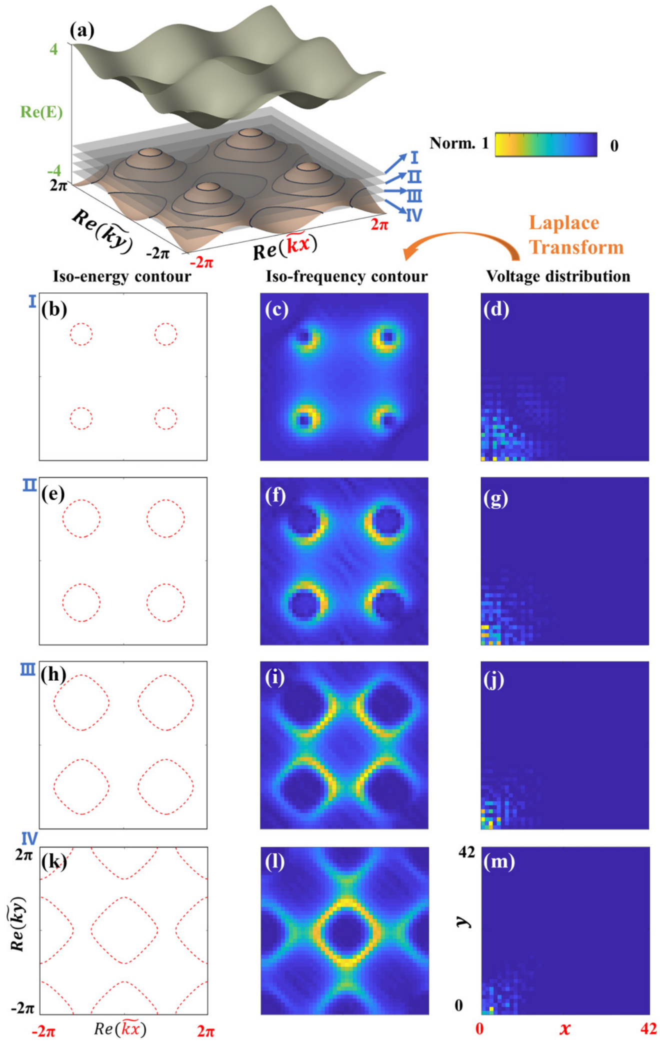

FIG. 8. Laplace transform characters GBZ. (a) Band structure of the effective non-Hamiltonian H with $\gamma = 0.5t$ in GBZ. I–IV denote the cut plane of the band structure with $E = 1.8$, 2.3, 2.8, 3.3, respectively. The intersections between the cut plane and the band structure are the isoenergy contours, which are individually shown in (b), (e), (h), and (k). (d), (g), (j), and (m) show the numerically calculated voltage response distribution of the NH circuit system (21 by 21 units) in real space with $Y_0 = i w_0 C_0$, where $C_0 =$ 18 nF, 23 nF, 28 nF, 33 nF, respectively. Here we adjust the eigenvalues of the systems with the self-admittance Y_0 to choose the bulk modes of interest. A pulse (not shown in figure) is injected into the center of the circuit to excite the voltage response, and their corresponding voltage distribution in GBZ after the Laplace transform are shown in (c), (f), (i), and (j). The voltage distribution is localized at the corner as a result of the NH corner effect. The imaginary parts of the complex vectors are $[{\rm Im}(\widetilde{k_x}), {\rm Im}(\widetilde{k_y})] = (\beta_0, \beta_0)$, $\beta_0 = \sqrt{|(t-\gamma)/(t+\gamma)|}$.

Given the wave function $\psi_{\tilde{k}}(r) = e^{i\tilde{k}x}u_{\tilde{k}}(x)$ from the generalized Bloch theory, one can always find a positive constant ξ such that $|u_{\tilde{k}}| \leqslant \xi$. Hence $\psi_{\tilde{k}}(r)$ is of exponential order $-{\rm Im}(\tilde{k})$. Then $\mathscr{L}[\psi_{\tilde{k}}(r)]$ exists for all s when (i) ${\rm Re}(s) \geqslant$

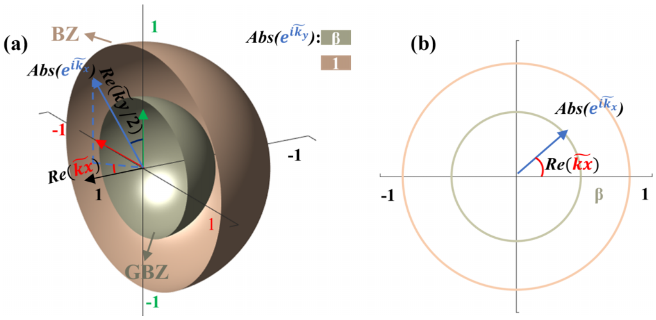

FIG. 9. Calculated Brillouin zone and generalized Brillouin zone. (a) Modulated phase factor $e^{i\mathbf{k}}$ and $e^{i\widetilde{\mathbf{k}}}$ in BZ and GBZ, respectively. $Abs(e^{i\widetilde{\mathbf{k}}}) = e^{-\mathrm{Im}(\widetilde{\mathbf{k}})}$, $Arg(e^{i\widetilde{\mathbf{k}}}) = \mathrm{Re}(\widetilde{\mathbf{k}})$. For a Hermitian system, $Abs(e^{i\widetilde{k}_n}) = 1, n = x, y$, which corresponds to the real wave vectors. In the GBZ, $Abs(e^{i\widetilde{\mathbf{k}}})$ determines the preference direction of the non-Bloch states, i.e., $|\beta_x| = |e^{i\widetilde{k}_x}| < 1$ and $|\beta_x| > 1$ correspond to the direction of $-x$ and x, and $|\beta_x| = 1$ suggests symmetric propagation of the Bloch wave. As indicated in the picture (gray sphere), our model prefers to propagate toward the bottom-left corner with constant $\mathrm{Im}(\widetilde{\mathbf{k}})$. In the Methods section, we consider a more complicated model whose $\mathrm{Im}(\widetilde{\mathbf{k}})$ varies. (b) Profile of the modulated phase factor with $\mathrm{Re}(i\widetilde{k}_y) = \frac{\pi}{2}$.

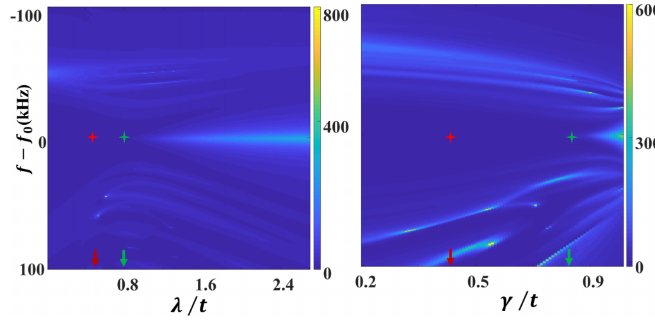

FIG. 10. Frequency scan of the impedance against ground at the corner from simulation. The color bar denotes the impedance value. The impedance peak at the resonance frequency f_0 indicates the presence of corner states. The red and the green arrows indicate the phase transition points predicted by the Bloch phase diagram and the non-Bloch one, respectively. The red and the green stars are the points where impedance resonance starts to occur, which are predicted by the Bloch phase diagram and the non-Bloch one. (a) $(\gamma, \lambda) = (0.6t, \lambda)$ and phase transition at $(\gamma, \lambda) = (0.6t, 0.8t)$; (b) $(\gamma, \lambda) = (\gamma, 0.6t)$ and phase transition at $(\gamma, \lambda) = (0.6t, 0.8t)$. Clearly, the non-Bloch phase diagram can correctly capture the phase transition.

$-\mathrm{Im}(\tilde{k})$, provided that $\psi_{\tilde{k}}(r)$ is right localized; (ii) $\mathrm{Re}(s) \leqslant -\mathrm{Im}(\tilde{k})$, provided that $\psi_{\tilde{k}}(r)$ is left-localized. We remark that $\mathscr{L}[\psi_{\tilde{k}}(r)]$ always exists in GBZ: $\mathrm{Re}(s) = -\mathrm{Im}(\tilde{k})$, and this might provide a general algorithm to calculate the high-dimensional GBZ. Figure 8 shows more numerical evidence for the GBZ demonstration with help of the Laplace transform.

APPENDIX C: GBZ CALCULATION

The previously reported studies on high-dimensional NH systems are restricted to fine-tuned models in which $Im(\widetilde{\mathbf{k}})$ is a constant, and there is no general approach to calculate the high-dimensional GBZ where $Im(\widetilde{\mathbf{k}})$ varies. In the Supplemental Material, we have developed a dimension-reducing approach for calculating the high-dimensional GBZ for more complicated systems. Using this approach we have calculated the GBZ of the proposed system (Fig. 9), achieving good agreement with the analytical solution where $Im(\widetilde{\mathbf{k}}) = (\beta_0, \beta_0)$, $\beta_0 = \sqrt{|(t-\gamma)/(t+\gamma)|}$. It is worth noting that the global material loss and scattering in the medium will attenuate the wave during propagation and can also lead to complex wave vectors. However, those wave vectors are still within the framework of conventional band theory and topology [1–4].

APPENDIX D: SECOND-ORDER TOPOLOGY REDEFINED IN GBZ

In Hermitian topolectrical circuits, this node impedance response is widely used to detect the presence of zero-energy topological boundary states [57–64], which locates at the band gap. However, we find that this approach to detect topological states cannot be generalized to NH topolectrical circuits unless (i) the eigenvalues of the topological boundary states are pinned to zero in the relatively large band gap; (ii) the eigenvalues of the circuit admittance are real numbers, not only because the complex eigenvalues lead the circuit to unstable states but also the pure imaginary eigenvalues of the bulk states interfere with the detection.

Here our model has a chiral symmetry $\sigma_z^{-1}J(w,\mathbf{k})\sigma_z = -J(w,\mathbf{k})$, which ensures that the eigenvalues appear in pairs $(-E, E)$ and the eigenvalues of the topological corner states are pinned to zero (corresponding to condition i). Besides, our model is also pseudo-Hermitian $\eta^{-1}J\eta = J$ with

$$\eta = \begin{pmatrix} 0 & 0 & \dots & 0 & \sigma_y \\ 0 & 0 & \dots & \sigma_y & 0 \\ \vdots & \vdots & \ddots & \vdots & \vdots \\ 0 & \sigma_y & \dots & 0 & 0 \\ \sigma_y & 0 & \dots & 0 & 0 \end{pmatrix}, \tag{D1}$$

and J is the circuit admittance under open boundary condition. The pseudo-Hermiticity of J ensures that all the eigenvalues are real [corresponding to condition (ii)]. So, in our circuit, the impedance peak around the corner at the resonance frequency is a definite and reliable indicator of the presence of corner states.

In the main article we have measured the impedance response of differently configurated topological circuits. For configuration $(\gamma, \lambda) = (0.5t, 2t)$, the measured response shows a strong impedance resonance around the circuit corner at LC frequency while no resonance for $(\gamma, \lambda) = (0.6t, 0.6t)$, suggesting $(\gamma, \lambda) = (0.5t, 2t)$ is a topological phase and $(\gamma, \lambda) = (0.6t, 0.6t)$ is a trivial phase. We compare the above experimental results to the phase diagrams and find the non-Bloch phase diagram can precisely capture the topological phases. Also, to avoid the finite-size effects due to the limited samples, we have picked a set of continuous parameter values and numerically calculated the impedance response as shown in Fig. 10. Those additional data provide further supports for our conclusion.

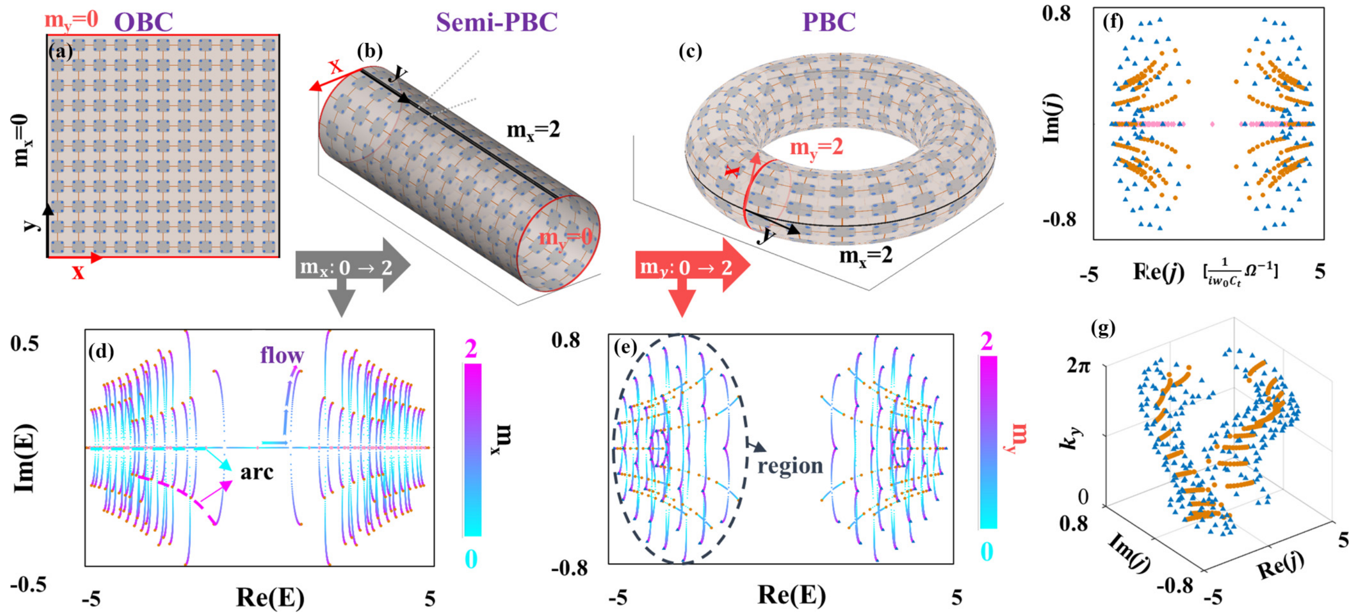

FIG. 11. Sensitivity of the non-Bloch band to the boundary condition. (a)–(c) Realization of different boundary conditions. (a) OBC, $(m_x, m_y) = (0, 0)$. (b) Semi-OBC, $(m_x, m_y) = (2, 0)$, which is periodic along x and open along y, respectively. (c) PBC, $(m_x, m_y) = (2, 2)$. (d) and (e) Spectral flow of H in the complex plane, which evolves from OBC, semi-OBC, to PBC. The blue-magenta flow represents OBC-PBC interpolation, which is quantified by one of the boundaries intracell hopping m_x or m_y. Dots with the same color (m_x or m_y is constant) indicate the spectrum of the system with the specific boundary. The pattern of the spectral distribution varies as the imposed boundary. (d) Flow from OBC (pink rhombi) to semi-PBC (orange dots). For the OBC and the semi-PBC, all the eigenvalues distribute on the several spectral arcs (only one arc is plotted). (e) Flow from semi-PBC to PBC (orange triangles), while for the PBC, the eigenvalues distribute evenly in the spectral region. (f) and (g) Measured complex admittance spectrum of $J_0(w_0, k)$, which emulates H. Each node of the circuit is grounded by a resistor $R = 51\ \Omega$ due to the stability consideration, thus $Y_0 = 1/R$. (f) Admittance spectrum of the OBC (pink rhombi), semi-PBC (orange dots), and PBC (orange triangles). (g) Admittance spectrum of the semi-PBC and the PBC in $j - k_y$ space. A prerequisite of the NH corner effect in our model is the OBC, since the Bloch wave behavior recovers along the periodic direction. Hence, for the semi-PBC and PBC, here $\mathrm{Im}(\widetilde{k}_y) = 0$.

APPENDIX E: SENSITIVITY TO BOUNDARY CONDITIONS

The Born–von Karman boundary theory suggests that the introduction of boundaries into a lattice will not significantly influence the bulk states (exceptions are given for edge states). However, the complex energy spectrum of a NH system can exhibit high sensitivity to the imposed boundary conditions. Unlike open boundary conditions (OBCs), periodic boundary conditions (PBCs) assume that the atoms around the boundary still have complete interaction with their neighbors, so they are ignorant of the boundary. For example, in our model, when $m_x (or\ m_y) = 2$, we have exact PBC along y (or x) that possesses translation symmetry, and we have OBC that breaks translational invariance when $m_x (or\ m_y) = 0$ [Figs. 11(a) and 11(c)]. To show this violation, we interpolate between the OBC and the PBC by adiabatically increasing the boundary hopping amplitude m_x or m_y from zero up to normal via complex fluxes [Figs. 11(d) and 11(e)]. This interpolation allows us to understand how the spectrum of our model evolves from OBCs to semi-OBCs to PBCs. As shown in Figs. 11(d) and 11(e), the OBC spectrum traces out arcs in the complex energy plane, and the pattern of the spectrum distribution is gradually deformed from an arclike shape to a regionlike shape under the aforementioned spectral flow evolution. Experimentally, to assess the different boundary conditions, the topolectrical circuits were "bent" as depicted in Figs. 11(a)–11(c). We note that, based on Kirchhoff's law, the deformations of the topolectrical circuits were achieved by simply wiring the desired nodes at the boundaries of the system. Figures 11(f) and 11(g) plot the corresponding measured admittance eigenvalues of the three systems. They show that the spectrum of the system with OBC differs drastically from those observed in the systems with PBC and semi-PBC. Note that $J_O BC$ with OBC has a real spectrum (all eigenvalues are real numbers) due to the pseudo-Hermitian $\eta^{-1} J \eta = J$.

APPENDIX F: EXPERIMENTAL MEASUREMENTS

In the main article, we employ temporal topolectrical circuits to emulate the NH dynamics in open systems. Therein, to demonstrate the non-Bloch evolution of the NH systems, which is the origin of the NH corner effect, we monitor the time-resolved voltage response over the time at each node after a Gaussian pulse current signal is injected into the center of the circuit. As shown in Figs. 1(d) and 1(e) in the main article, the node voltage propagates chirally toward the corner with increasing amplitude, verifying the non-Bloch dynamics. To get the time-resolved voltage response, one needs to measure all the voltage at each node simultaneously after the pulse has been injected, e.g., for our circuit, we need to measure 11*11*4 nodes simultaneously, which is not feasible. Instead of simultaneous measurement, we decompose this into 11*11*4 times individual measurements. In the following we

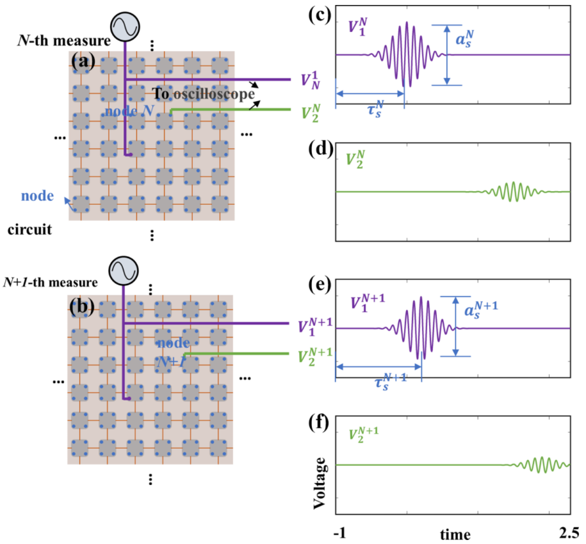

FIG. 12. Schematics of the time-resolved voltage response: (a) nth measurement, (c) input Gaussian pulse signal, and (d) node N voltage response for Nth measurement. (b) N+1-th measurement. (e) Input Gaussian pulse signal and (f) node $N+1$ voltage response for $N+1$-th measurement.

detail two of the individual measurements for illustrating (see Fig. 12).

For the Nth measurement, we record the input pulse and the voltage response at node N. The same procedure repeats for the N+1-th measure, except that the voltage response at node $N+1$ is recorded. The departure time and amplitude of the input pulse may vary during the individual measurements (e.g., $\tau_s^{(N+1)} \neq \tau_s^N$, $a_s^{(N+1)} \neq a_s^N$). However, the group delay and the ratio amplitude between pulse and the response are constant because they are determined by the intrinsic property of the circuit (e.g., the group delay and ratio amplitude between V_2^N and V_1^N). Hence we can use the input pulse recorded each time to calibrate (normalize) the voltage response of the nodes:

$$V_2'^{N+1}(t) = V_2^{N+1}\left(\tau_s^{N+1} - \tau_s^N + t\right)\frac{a_s^{N+1}}{a_s^N}. \tag{F1}$$

With all calibrated node voltage responses, one can finally obtain the time-resolved voltage signals of the topolectrical circuits that respond to a "single" Gaussian pulse. The videos appended show the measured time-dependent voltage distribution when a pulse is injected to the center of the circuit. (The first video is of the Hermitian circuit, while the second video is of the non-Hermitian circuit.)

[1] M. Z. Hasan and C. L. Kane, Rev. Mod. Phys. **82**, 3045 (2010).
[2] X.-L. Qi and S.-C. Zhang, Rev. Mod. Phys. **83**, 1057 (2011).
[3] T. Ozawa, H. M. Price, A. Amo, N. Goldman, M. Hafezi, L. Lu, M. C. Rechtsman, D. Schuster, J. Simon, O. Zilberberg, and I. Carusotto, Rev. Mod. Phys. **91**, 015006 (2019).
[4] L. Lu, J. D. Joannopoulos, and M. Soljačić, Nature Photon **8**, 821 (2014).
[5] E. J. Bergholtz, J. C. Budich, and F. K. Kunst, Rev. Mod. Phys. **93**, 015005 (2021).
[6] L. Feng, R. El-Ganainy, and L. Ge, Nat. Photonics **11**, 752 (2017).
[7] M.-A. Miri and A. Alù, Science **363**, eaar7709 (2019).
[8] V. Kozii and L. Fu, arXiv:1708.05841.
[9] Y. Nagai, Y. Qi, H. Isobe, V. Kozii, and L. Fu, Phys. Rev. Lett. **125**, 227204 (2020).
[10] Y.-L. Tao, T. Qin, and Y. Xu, Phys. Rev. B **107**, 035140 (2023).
[11] C. E. Rüter, K. G. Makris, R. El-Ganainy, D. N. Christodoulides, M. Segev, and D. Kip, Nat. Phys. **6**, 192 (2010).
[12] Y. Li, C. Fan, X. Hu, Y. Ao, C. Lu, C. T. Chan, D. M. Kennes, and Q. Gong, Phys. Rev. Lett. **129**, 053903 (2022).
[13] B. Zhen, C. W. Hsu, Y. Igarashi, L. Lu, I. Kaminer, A. Pick, S.-L. Chua, J. D. Joannopoulos, and M. Soljačić, Nature (London) **525**, 354 (2015).
[14] M. Wu, R. Peng, J. Liu, Q. Zhao, and J. Zhou, Phys. Rev. Lett. **125**, 137703 (2020).
[15] Z. Gong, Y. Ashida, K. Kawabata, K. Takasan, S. Higashikawa, and M. Ueda, Phys. Rev. X **8**, 031079 (2018).
[16] K. Wang, A. Dutt, C. C. Wojcik, and S. Fan, Nature (London) **598**, 59 (2021).
[17] K. Wang, A. Dutt, K. Y. Yang, C. C. Wojcik, J. Vučković, and S. Fan, Science **371**, 1240 (2021).
[18] D. Leykam, S. Flach, and Y. D. Chong, Phys. Rev. B **96**, 064305 (2017).
[19] S. Diehl, E. Rico, M. A. Baranov, and P. Zoller, Nat. Phys. **7**, 971 (2011).
[20] F. Song, S. Yao, and Z. Wang, Phys. Rev. Lett. **123**, 170401 (2019).
[21] V. M. Martinez Alvarez, J. E. Barrios Vargas, and L. E. F. Foa Torres, Phys. Rev. B **97**, 121401(R) (2018).
[22] W. Zhu, W. X. Teo, L. Li, and J. Gong, Phys. Rev. B **103**, 195414 (2021).
[23] W. Wang, X. Wang, and G. Ma, Nature **608**, 50 (2022).
[24] G. Harari, M. A. Bandres, Y. Lumer, M. C. Rechtsman, Y. D. Chong, M. Khajavikhan, D. N. Christodoulides, and M. Segev, Science **359**, eaar4003 (2018).
[25] M. A. Bandres, S. Wittek, G. Harari, M. Parto, J. Ren, M. Segev, D. N. Christodoulides, and M. Khajavikhan, Science **359**, eaar4005 (2018).
[26] H. Zhao, X. Qiao, T. Wu, B. Midya, S. Longhi, and L. Feng, Science **365**, 1163 (2019).
[27] Y. Xiong, J. Phys. Commun. **2**, 035043 (2018).
[28] S. Yao and Z. Wang, Phys. Rev. Lett. **121**, 086803 (2018).
[29] S. Longhi, Phys. Rev. Res. **1**, 023013 (2019).
[30] D. S. Borgnia, A. J. Kruchkov, and R.-J. Slager, Phys. Rev. Lett. **124**, 056802 (2020).
[31] K. Zhang, Z. Yang, and C. Fang, Phys. Rev. Lett. **125**, 126402 (2020).
[32] L. Li, C. H. Lee, S. Mu, and J. Gong, Nat. Commun. **11**, 5491 (2020).
[33] N. Okuma, K. Kawabata, K. Shiozaki, and M. Sato, Phys. Rev. Lett. **124**, 086801 (2020).
[34] R. Okugawa, R. Takahashi, and K. Yokomizo, Phys. Rev. B **102**, 241202(R) (2020).

[35] L. Zhang, Y. Yang, Y. Ge, Y.-J. Guan, Q. Chen, Q. Yan, F. Chen, R. Xi, Y. Li, D. Jia *et al.*, Nat. Commun. **12**, 6297 (2021).
[36] X. Zhang, Y. Tian, J.-H. Jiang, M.-H. Lu, and Y.-F. Chen, Nat. Commun. **12**, 5377 (2021).
[37] K. Zhang, Z. Yang, and C. Fang, Nat. Commun. **13**, 2496 (2022).
[38] K. Yokomizo and S. Murakami, Phys. Rev. Lett. **123**, 066404 (2019).
[39] Z. Yang, K. Zhang, C. Fang, and J. Hu, Phys. Rev. Lett. **125**, 226402 (2020).
[40] R. Okugawa, R. Takahashi, and K. Yokomizo, Phys. Rev. B **103**, 205205 (2021).
[41] K. Yokomizo and S. Murakami, arXiv:2210.04412.
[42] Y. Yi and Z. Yang, Phys. Rev. Lett. **125**, 186802 (2020).
[43] L. Jin and Z. Song, Phys. Rev. B **99**, 081103(R) (2019).
[44] L. Xiao, T. Deng, K. Wang, G. Zhu, Z. Wang, W. Yi, and P. Xue, Non-Hermitian bulk–boundary correspondence in quantum dynamics, Nat. Phys. **16**, 761 (2020).
[45] S. Yao, F. Song, and Z. Wang, Phys. Rev. Lett. **121**, 136802 (2018).
[46] T. Liu, Y.-R. Zhang, Q. Ai, Z. Gong, K. Kawabata, M. Ueda, and F. Nori, Phys. Rev. Lett. **122**, 076801 (2019).
[47] M. Wu, M. Weng, Q. Zhao, Y. Meng, and J. Zhou, arXiv:2206.11547.
[48] X.-Q. Sun, S.-C. Zhang, and T. c. v. Bzdušek, Phys. Rev. Lett. **121**, 106402 (2018).
[49] Q. Wu, A. A. Soluyanov, and T. Bzdušek, Science **365**, 1273 (2019).
[50] G. Lindblad, Commun. Math. Phys. **48**, 119 (1976).
[51] F. Song, S. Yao, and Z. Wang, Phys. Rev. Lett. **123**, 246801 (2019).
[52] See Supplemental Material at http://link.aps.org/supplemental/10.1103/PhysRevB.107.064307 for details about (1) derivation of the effective non-Hermitian Hamiltonian, (2) temporal topolectical circuits, (3) experimental measurements, (4) GBZ calculation, and (5) caption of video S.1 and S.2. It includes Refs. [38,58,59,62,63,65,66].
[53] W. A. Benalcazar, B. A. Bernevig, and T. L. Hughes, Science **357**, 61 (2017).
[54] M. Serra-Garcia, V. Peri, R. Süsstrunk, O. R. Bilal, T. Larsen, L. G. Villanueva, and S. D. Huber, Nature (London) **555**, 342 (2018).
[55] C. W. Peterson, W. A. Benalcazar, T. L. Hughes, and G. Bahl, Nature (London) **555**, 346 (2018).
[56] J. Cserti, G. Széchenyi, and G. Dávid, J. Phys. A: Math. Theor. **44**, 215201 (2011).
[57] C. H. Lee, S. Imhof, C. Berger, F. Bayer, J. Brehm, L. W. Molenkamp, T. Kiessling, and R. Thomale, Commun. Phys. **1**, 39 (2018).
[58] T. Hofmann, T. Helbig, C. H. Lee, M. Greiter, and R. Thomale, Phys. Rev. Lett. **122**, 247702 (2019).
[59] T. Helbig, T. Hofmann, S. Imhof, M. Abdelghany, T. Kiessling, L. Molenkamp, C. Lee, A. Szameit, M. Greiter, and R. Thomale, Nat. Phys. **16**, 747 (2020).
[60] J. Bao, D. Zou, W. Zhang, W. He, H. Sun, and X. Zhang, Phys. Rev. B **100**, 201406(R) (2019).
[61] J. Ningyuan, C. Owens, A. Sommer, D. Schuster, and J. Simon, Phys. Rev. X **5**, 021031 (2015).
[62] N. A. Olekhno, E. I. Kretov, A. A. Stepanenko, P. A. Ivanova, V. V. Yaroshenko, E. M. Puhtina, D. S. Filonov, B. Cappello, L. Matekovits, and M. A. Gorlach, Nat. Commun. **11**, 1436 (2020).
[63] S. Imhof, C. Berger, F. Bayer, J. Brehm, L. W. Molenkamp, T. Kiessling, F. Schindler, C. H. Lee, M. Greiter, T. Neupert *et al.*, Nat. Phys. **14**, 925 (2018).
[64] P. M. Lenggenhager, A. Stegmaier, L. K. Upreti, T. Hofmann, T. Helbig, A. Vollhardt, M. Greiter, C. H. Lee, S. Imhof, H. Brand *et al.*, Nat. Commun. **13**, 4373 (2022).
[65] W. Zhang, D. Zou, Q. Pei, W. He, J. Bao, H. Sun, and X. Zhang, Phys. Rev. Lett. **126**, 146802 (2021).
[66] W. Zhang, H. Yuan, N. Sun, H. Sun, and X. Zhang, Nat. Commun. **13**, 2937 (2022).
[67] Q. Zhao, J. Zhou, F. Zhang, and D. Lippens, Mater. Today **12**, 60 (2009).
[68] R. Peng, Z. Xiao, Q. Zhao, F. Zhang, Y. Meng, B. Li, J. Zhou, Y. Fan, P. Zhang, N.-H. Shen *et al.*, Phys. Rev. X **7**, 011033 (2017).
[69] I. De Leon and F. S. Roux, Phys. Rev. B **71**, 235105 (2005).
[70] B. Yang, Q. Guo, B. Tremain, R. Liu, L. E. Barr, Q. Yan, W. Gao, H. Liu, Y. Xiang, J. Chen *et al.*, Science **359**, 1013 (2018).
[71] Y. Yang, Z. Gao, H. Xue, L. Zhang, M. He, Z. Yang, R. Singh, Y. Chong, B. Zhang, and H. Chen, Nature (London) **565**, 622 (2019).
[72] L. Debnath and D. Bhatta, *Integral Transforms and Their Applications* (Chapman and Hall/CRC, Boca Raton, FL, 2016).
[73] C. H. Lee and R. Thomale, Phys. Rev. B **99**, 201103(R) (2019).
[74] D. Zou, T. Chen, W. He, J. Bao, C. H. Lee, H. Sun, and X. Zhang, Nat. Commun. **12**, 7201 (2021).
[75] W. Zhang, F. Di, H. Yuan, H. Wang, X. Zheng, L. He, H. Sun, and X. Zhang, Phys. Rev. B **105**, 195131 (2022).
[76] C. Shang, S. Liu, R. Shao, P. Han, X. Zang, X. Zhang, K. N. Salama, W. Gao, C. H. Lee, R. Thomale *et al.*, Advanced Science **9**, 2202922 (2022).
[77] M. Aidelsburger, M. Atala, M. Lohse, J. T. Barreiro, B. Paredes, and I. Bloch, Phys. Rev. Lett. **111**, 185301 (2013).
[78] R. Keil, C. Poli, M. Heinrich, J. Arkinstall, G. Weihs, H. Schomerus, and A. Szameit, Phys. Rev. Lett. **116**, 213901 (2016).